International Journal of Multiphase Flow 36 (2010) 397–405

Contents lists available at ScienceDirect

International Journal of Multiphase Flow

journal homepage: www.elsevier.com/locate/ijmulflow

Droplet dynamics in a bifurcating channel

A. Carlson *, M. Do-Quang, G. Amberg

Department of Mechanics, Linné Flow Center, The Royal Institute of Technology, Osquars Backe 18, 11428 Stockholm, Sweden

ARTICLE INFO

Article history:
Received 21 July 2009
Received in revised form 16 December 2009
Accepted 5 January 2010
Available online 11 January 2010

Keywords:
Droplet dynamics
Cahn–Hilliard
Bifurcating channels
Wetting
Rayleigh–Plateau instability
Passive breakup

ABSTRACT

In the present paper we present a phenomenological description of droplet dynamics in a bifurcating channel that is based on three-dimensional numerical experiments using the Phase Field theory. Droplet dynamics is investigated in a junction, which has symmetric outflow conditions in its daughter branches. We identify two different flow regimes as the droplets interact with the tip of the bifurcation, *splitting* and *non-splitting*. A distinct criterion for the flow regime transition is found based on the initial droplet volume and the Capillary (*Ca*) number. The Rayleigh–Plateau instability is identified as a driving mechanism for the droplet breakup close to the threshold between the splitting and non-splitting regime.

1. Introduction

Droplet dynamics is a very common phenomenon that can be observed in everyday life, for instance during rainfall and in your kitchen sink. Due to their ubiquitous occurrence with fascinating physical phenomena they have attracted the attention of scientists for more than a century. Nonetheless, many flows involving droplets are yet not fully understood. This is a direct consequence of the complex physical picture formed by the competition between hydrodynamic and free-surface forces, in addition to the wetting phenomenon that governs the nature of the interaction between the interface and the solid surface.

During the last decade there has been a rapid growth of droplet microfluidic applications, which has resulted in an increased interest in flow physics at the micro scale. In these applications it is of utmost importance to obtain well-defined droplet behaviors as they traverse geometrically complex networks of channels.

One avenue of droplet microfluidics is the use of droplets as compartments for a desired physical phenomenon such as mixing, as shown by Garstecki et al. (2005). Mixing in micro scale is a well-known obstacle, since it is merely driven by molecular diffusion. One direction to follow in order to foster mixing is emulsion, which can be realized by design of droplet–droplet interaction. The potential use of an emulsion technique is often limited by the possibility to precisely control the droplets size distribution. Passive droplet formation, in a device requiring no moving parts, have been demonstrated in a flow focusing device by Anna et al. (2003) and by geometrically mediated droplet division in a λ junction (Menetrier-Deremble and Tabeling, 2006) and droplet formation in T-junctions (Link et al., 2004). Droplets can also be introduced in microfluidic devices to perform specific tasks, where they have shown promise as flow parameters to perform logical operations (Prakash and Gershenfeld, 2007) and used to code/decode various signals (Fuerstman et al., 2007).

The importance of understanding droplet and bubble dynamics in complex networks goes well beyond its relevance to design and applications in microfluidic technology. They are also widely encountered in medical technology, where they are used as vehicles for drug transport, part of medical treatment strategies (gas embolotherapy) or an undesired bi-product of a clinical treatment (air embolism). Air embolism occurs as an air bubble enters the vascular system that may have a dangerous or even fatal outcome, if appropriate measures are not taken. As the bubble traverses through the vascular system it might lodge in one of its micro-circulations occluding the natural blood flow, causing ischemia (Bull, 2005). If a bubble should be trapped in one of the critical sections in the body such as a capillary in the brain or in a coronary circulation the outcome could be disastrous. Embolotherapy on the other hand is a medical treatment strategy that exploits bubbles and their free surfaces (Bull, 2005), where a bubble is introduced in order to occlude the blood flow to certain parts of the tissue thus excluding its oxygen supply.

The medical relevance of embolism and embolotherapy has initiated experimental investigations of bubbles in artery and capillary geometries (Calderon et al., 2005; Calderon et al., 2006; Eshpuniyani et al., 2005), in an attempt to predict which blood vessel it will occlude. Different flow regimes for bubble splitting and

* Corresponding author.
E-mail address: andreaca@mech.kth.se (A. Carlson).

0301-9322/$ - see front matter © 2010 Elsevier Ltd. All rights reserved.
doi:10.1016/j.ijmultiphaseflow.2010.01.002

lodging were observed. Eshpuniyani et al. (2005) found the non-splitting bubbles to be sensitive to gravity, with regard to which branch it would choose to lodge into. Baroud et al. (2006) made a similar observation about the disturbance sensitive nature of slug flow in a symmetric Y-junction. For velocities above a certain threshold the long, low viscous, liquid plugs divided asymmetrically as they propagated into a junction that was filled with air. The initial perturbation was believed to originate from a small imperfection, near the tip of the bifurcation, in the fabrication of the channel, as the fastest finger was always associated with the same branch.

In contrast to the vast amount of experimental results on droplet and bubble transport in complex geometries the literature on numerical experiments is scarce. Historically, computational multifluid dynamics has been restricted to rather simple geometries. As a result there is available today a great deal of knowledge about droplet and bubble dynamics in straight pipes and channels (Bretherton, 1961; Taylor, 1960; Aussillous and Quere, 2000). Numerical prediction of two-phase flows in T-junctions have been previously demonstrated by van der Graaf et al. (2006) with the Lattice Boltzman method and, low resolution simulations, performed by De Menech et al. (2008) and De Menech (2006) with the Phase Field method. We recognize that numerical results on droplet dynamics in Y-junctions are elusive. Manga (1996) investigated the motion of drops in a Y-junction with equally sized daughter branches with the boundary-integral method (Pozrikidis, 2001). He based his analysis on the assumption of a channel flow of Stokes type ($Re \ll 1$). His two-dimensional simulation results indicated that the drops have a tendency to follow the channel branch with the highest flow rate, and that two drops could interact at the tip of the bifurcation. Such a droplet–droplet interaction points at a plausible mixing effect by emulsification.

In order to numerically capture all physical aspects of droplet dynamics in complex geometries there are several obstacles that need to be overcome both in terms of modeling and in the numerical treatment. First, such simulations should rest on a physically sound description and numerically consistent treatment of complex wetting phenomena and free-surface forces. The computational technology needs to be able to handle two or more phases with different densities and viscosities that undergo topology changes such as droplet breakup. We also need the capability to deal with numerical domains of unstructured meshes. Solving the Cahn–Hilliard and the Navier Stokes equations with a finite element method appears as a computational platform realizing these requirements, opening a window of opportunity for numerical experiments on interfacial dynamics in complex geometries.

In the present paper we aim to elucidate parts of the physics governing droplet dynamics in bifurcating channels. Our investigation is based on three-dimensional numerical experiments by solving the Cahn–Hilliard and the Navier Stokes equations with a finite element method. A multiphase flow consisting of two binary immiscible liquids is simulated in a bifurcating channel, which is frequently encountered in medical technology and microfluidic applications.

We seek in particular to define the parameter range that controls the resulting droplet dynamics. In other words, for what critical condition does the droplet split or not as it interacts with the tip of the bifurcation. To reduce the number of parameters that might affect such phenomena and to isolate effects from the capillary force, we consider here two phases with equal density and viscosity. In what follows we will show that a type of Rayleigh–Plateau instability, which is not captured in two-dimensional simulations (Pozrikidis, 2001), can be a driving mechanism for droplet breakup. Two distinct flow regimes are characterized, splitting and non-splitting droplets. A relation between the two regimes has been identified, based on the initial droplet size and the Capillary (Ca) number. We find the non-splitting flow regime to inherit an unstable nature, which has a direct impact on the mass flow distribution in the channel branches.

2. Mathematical formulation

2.1. The Phase Field theory

The Phase Field theory is based on the thermodynamical consideration of the free energy of a binary system. The two components are here assumed to be immiscible and separated by a narrow diffuse interfacial region. By considering that two immiscible components actually mix over an interfacial region van der Waals (1893) proposed the idea of a diffuse interface. The composition profile of the interface can be seen as the competition between the random molecular motion and the molecular attraction.

Cahn and Hilliard (1958) derived the free energy by making a multivariable Taylor expansion about the free energy per molecule,

$$f = \beta\Psi(C) + \frac{\alpha}{2}|\nabla C|^2, \tag{1}$$

following here the Phase Field derivation and notation by Jacqmin (1999), where C is an order parameter. The creation of an interface is established by the competition between the bulk free energy $\beta\Psi(C)$, and the interfacial energy $\frac{\alpha}{2}|\nabla C|^2$ due to composition variations. α and β are constants that comes out directly from the Taylor expansion, see Cahn and Hilliard (1958), and are proportional to the surface tension coefficient σ and the interface width ϵ, $\beta \sim \frac{\sigma}{\epsilon}$ and $\alpha \sim \sigma\epsilon$. The free energy functional Ψ and the Phase Field parameters α, β and the mobility M control the interfacial dynamics and width. Ψ is taken as a double-well function, $\Psi(C) = \frac{1}{4}(C+1)^2(C-1)^2$, which will give the two equilibrium states at $C = \pm 1$. Integration over the volume of the systems gives the total free energy defined by $F = \int_\Omega f\, dV$. The functional derivative of F with respect to the order parameter C gives rise to the chemical potential,

$$\phi = \frac{\delta F}{\delta C} = \beta\Psi'(C) - \alpha\nabla^2 C. \tag{2}$$

By minimizing the chemical potential with respect to C we obtain the equilibrium profile to the interface, here given in one dimension as $C_0(x) = \tanh\left(\frac{x}{\sqrt{2}\epsilon}\right)$. $\epsilon = \sqrt{\frac{\alpha}{\beta}}$ is the mean field thickness and the surface tension is defined by the integral,

$$\sigma = \alpha\int_{-\infty}^{\infty}\left(\frac{dC_0}{dx}\right)^2 dx = \frac{2\sqrt{2}}{3}\alpha^{\frac{1}{2}}\beta^{\frac{1}{2}}. \tag{3}$$

By taking into account the effects of the fluids motion a convection–diffusion equation is obtained, also referred to as the Cahn–Hilliard equation

$$\frac{\partial C}{\partial t} + \mathbf{u}\cdot\nabla C = \nabla\cdot(M\nabla\phi) = \nabla\cdot(M\nabla(\beta\Psi'(C) - \alpha\nabla^2 C)), \tag{4}$$

where the mobility M is considered as a constant. We require that there is no flux of the chemical potential through the boundaries of the domain, which is fulfilled by the Neumann boundary condition

$$\frac{\partial\phi}{\partial\mathbf{n}} = 0, \tag{5}$$

where $\mathbf{n}$ is the normal vector to the boundary. The surface free energy contribution is postulated as (Carlson et al., 2009)

$$F_{wall} = \int[\sigma_{SL} + (\sigma_{SV} - \sigma_{SL})g(C)]dA, \tag{6}$$

where $\sigma_{()}$ is the surface energy between the three different phases; liquid (L), gas (V) and solid (S). $g(C) = 0.5 + 0.75C - 0.25C^3$ is a

smooth function between zero and one, and its derivative $g'(C)$ will be non-zero only at the diffuse contact line. In Eq. (6) it is assumed that the interface is at or close to equilibrium as it wets the solid surface. θ_0 is the equilibrium contact angle, formed between the tangent of the interface and the solid surface, given by Young's Law; $\cos(\theta_0) = \frac{\sigma_{SV}-\sigma_{SL}}{\sigma}$. Through the variational derivative of the total free energy of the system, with respect to C, and integration by parts, the natural boundary condition for the concentration at the wall is obtained,

$$\alpha \frac{\partial C}{\partial \mathbf{n}} + \sigma \cos(\theta_0) g'(C) = 0, \tag{7}$$

governing the diffusively controlled wetting at local equilibrium (Carlson et al., 2009).

2.2. Governing equations for the motion of the fluids

Both phases are considered as incompressible in an isothermal system,

$$\nabla \cdot \mathbf{u} = 0. \tag{8}$$

The interfacial two-phase flow is governed by Navier Stokes equations,

$$\rho\left(\frac{\partial \mathbf{u}}{\partial t} + (\mathbf{u}\cdot\nabla)\mathbf{u}\right) = -\nabla P + \nabla\cdot(\mu(\nabla\mathbf{u} + (\nabla\mathbf{u})^T)) - C\nabla\phi, \tag{9}$$

where $\mathbf{u}$ is the velocity and P is the modified pressure (Jacqmin, 1999). ρ and μ are the fluids density and dynamic viscosity, which are equal in both phases. The last term is expressing the surface tension force that is based on the model proposed by Jacqmin (1999). We impose a no-slip boundary condition at the wall $\mathbf{u} = 0$ and prescribe a velocity profile at the inlet with the shape of a paraboloid. To obtain a well-posed problem we apply a Neumann boundary condition on the pressure at the inlet,

$$\frac{\partial P}{\partial \mathbf{n}} = 0. \tag{10}$$

At the outlets the pressure is defined with an essential boundary condition $P = 0$, and a Neumann boundary condition is used for the velocities,

$$\frac{\partial \mathbf{u}}{\partial \mathbf{n}} = 0. \tag{11}$$

2.3. Scaling laws

The governing equations are made dimensionless based on the characteristic parameters of the flow, giving the dimensionless variables (denoted by $*$)

$$x = L_c x^*, \quad t = \frac{L_c}{U} t^*, \quad P = \rho U^2 P^*, \quad u = U u^*, \quad \phi = \frac{3\sigma}{2\sqrt{2}\epsilon}\phi^* \tag{12}$$

where L_c is a characteristic length scale and U is the reference velocity. By introducing this scaling into the Navier Stokes and Cahn–Hilliard equations we obtain their non-dimensional form, where the $*$ notation is left out,

$$\nabla \cdot \mathbf{u} = 0, \tag{13}$$

$$\frac{\partial C}{\partial t} + \mathbf{u}\cdot\nabla C = \frac{1}{Pe}\nabla^2\phi = \frac{1}{Pe}\nabla^2(\Psi'(C) - Cn^2\nabla^2 C), \tag{14}$$

$$\rho\left(\frac{\partial \mathbf{u}}{\partial t} + (\mathbf{u}\cdot\nabla)\mathbf{u}\right) = -\nabla P + \frac{1}{Re}\left(\nabla\cdot(\mu(\nabla\mathbf{u} + (\nabla\mathbf{u})^T)) - \frac{C\nabla\phi}{Cn\cdot Ca}\right). \tag{15}$$

Here four non-dimensional numbers appear:

$$Pe = \frac{2\sqrt{2}U\epsilon L_c}{3M\sigma}, \quad Cn = \frac{\epsilon}{L_c}, \quad Re = \frac{\rho U L_c}{\mu}, \quad Ca = \frac{2\sqrt{2}\mu U}{3\sigma}. \tag{16}$$

The Peclet (Pe) number expresses the ratio between advection and diffusion. The Cahn (Cn) number expresses the ratio between the interface width and the characteristic length scale. The Reynolds (Re) number expresses the ratio between the inertia and the viscous force. The Capillary (Ca) number expresses the ratio between the viscous and the surface tension force.

2.4. Computational technology

2.4.1. The numerical toolbox femLego

The computations have been carried out using the numerical toolbox femLego (Amberg et al., 1999), a symbolic tool for solving partial differential equations. The user has full control over the mathematical modeling and the numerical solution procedure as the partial differential equations, boundary conditions and numerical solvers are all defined in a single Maple worksheet. The code inherits adaptive mesh refinement and parallel computation capabilities (Do-Quang et al., 2007).

Due to the stiff nature of the Cahn–Hilliard equation, great care needs to be taken in the solution procedure in order to avoid numerical instabilities. The equation is treated and solved in accordance with Villanueva and Amberg (2006) with a type of preconditioned Conjugate Gradient (CG) method. The Navier Stokes equations are solved using a projection scheme, proposed by Guermond and Quartapelle (1997). The non-linear convective term is treated semi-implicitly permitting larger time steps during the computations, its linear systems for the velocities and pressure are, respectively, solved with a Generalized Minimal Residual method and a CG method. A first order forward Euler scheme has been applied for the time marching and all variables are discretized in space using piecewise linear functions.

2.5. Model validation

2.5.1. The Laplace law

In order to assure that the mathematical modeling in three dimensions is correctly implemented it has been validated against the Laplace law. The Laplace law gives an analytical expression for the pressure difference inside and outside of a static droplet or bubble submerged in a liquid. This test does in particular concern the treatment of the surface tension force that is directly balanced by the pressure force.

We have measured the pressure jump for different mesh spacing and Cn numbers. The Cn number gives the ratio between the width of the diffuse interface and the characteristic length scale in the flow, here being the droplet diameter d. The results are summarized in Table 1, where we have kept the $Ca = 1$, $Pe = 3\times10^{-3}$ and $Re = 1$ fixed. These dimensionless numbers gives an analytical pressure difference $(\Delta P)_{\text{analytical}} = 8\sqrt{2}/3$. The numerical domain has an extension of $[2d \times 2d \times 2d]$ and an equidistant mesh has been applied. Table 1 is summarizing the relative error between the computed and analytical pressure prediction for different Cn numbers and mesh spacings, after eight time steps. It is noted that

Table 1
Deviation between the numerical and analytical pressure for different Cn numbers and mesh resolutions. Δx is the mesh spacing and P_{error} is defined as the relative error between the analytically and the numerically predicted pressure jump, $P_{error} = 100\cdot\left(1 - \frac{(\Delta P)_{\text{numerical}}}{(\Delta P)_{\text{analytical}}}\right)$.

Cn	0.04	0.04	0.06	0.08
Δx	0.013	0.02	0.02	0.027
P_{error} (%)	0.6	2.0	0.6	0.9

the correct pressure is immediately obtained with good agreement between the numerical and analytical solution. One trend in Table 1 is that the error in pressure depends on the numerical resolution of the interface. Another observation is that the correct pressure jump is obtained even with wide interfaces.

2.5.2. Deformation of a droplet in Couette flow

The dynamic behavior of the surface tension force has also been verified by validating the numerical solution of the deformation of a three-dimensional droplet in a Couette flow. Taylor (1934) derived analytically the deformation (D) of a droplet in a shear flow in the limit of low Re numbers ($Re \ll 1$), which he also verified in experiments,

$$D = \frac{19\lambda + 16}{16\lambda + 16} Ca = \frac{L - B}{L + B}. \tag{17}$$

Here the viscosity ratio of the two liquids is λ, L and B are the major and minor axes, respectively. The Ca number $Ca = \frac{\mu\dot{\gamma}d}{\sigma}$ is defined by the shear rate $\dot{\gamma}$, μ the viscosity of the continuous liquid and d the droplet diameter. The deformation parameter D can be extracted from experiments and numerical simulations by measuring the major and minor axis when the droplet has reached steady-state. A two-dimensional sketch of the domain and a schematic description of the droplets minor (B) and major (L) axis is given in Fig. 1. Initially the droplet is spherical and it deforms into an ellipsoidal shape.

Table 2 gives the relative difference between the analytical and numerical results for a droplet in a Couette flow for various Ca numbers. All results are found to be in good agreement with the analytical prediction from Taylor given in Eq. (17). Fig. 2 shows the velocity vectors in a plane extracted at the center of the domain with a normal $[0 \cdot \bar{e}_x, 0 \cdot \bar{e}_y, 1 \cdot \bar{e}_z]$ and the iso-surface of $C = 0$ is describing the droplet shape. The simulation has reached steady-state, meaning that the capillary force balances the viscous force acting on the droplet. Three stagnation points are observed in the extracted plane, one at the center of the droplet and the two others are symmetrically placed at the left and right side of the droplet, see Fig. 2.

2.6. Geometrical description of the domain

Droplet dynamics is investigated in a three-dimensional Y-junction described by the two-dimensional sketch given in Fig. 3, where the z-direction goes into the plane of the figure. A velocity profile with a shape of a paraboloid, with a non-dimensional mean velocity $\bar{u} = 1$, has been prescribed at the inlet of the parent channel, and a Neumann boundary condition is defined for the pressure. A symmetric outlet condition is given for the pressure ($P = 0$) at the upper and lower daughter branch. The parent channel has a quadratic cross section L^2, L being the width of the channel, and

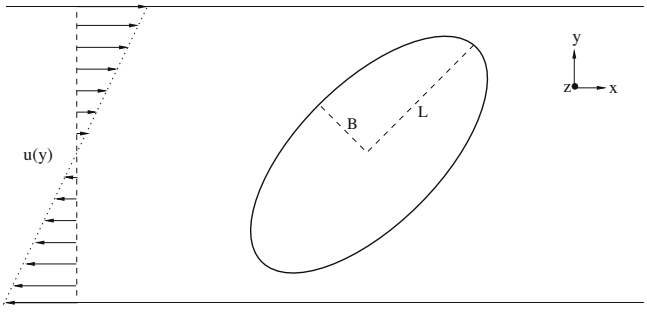

Fig. 1. Illustration of the Couette flow and a description of the minor (B) and major (L) axis of a droplet at steady-state.

Table 2
The relative deviation between the analytical and computed deformation parameter is given for different Ca numbers. All other parameters have been kept constant $Re = 0.01$, $Pe = 10^3$, $Cn = 0.06$ and $\lambda = 1$ and the mesh is equidistant with a spacing $\Delta x = 0.02$.

Ca	0.15	0.1	0.08	0.06
D_{error} (%)	2.8	1.1	0.8	1.0

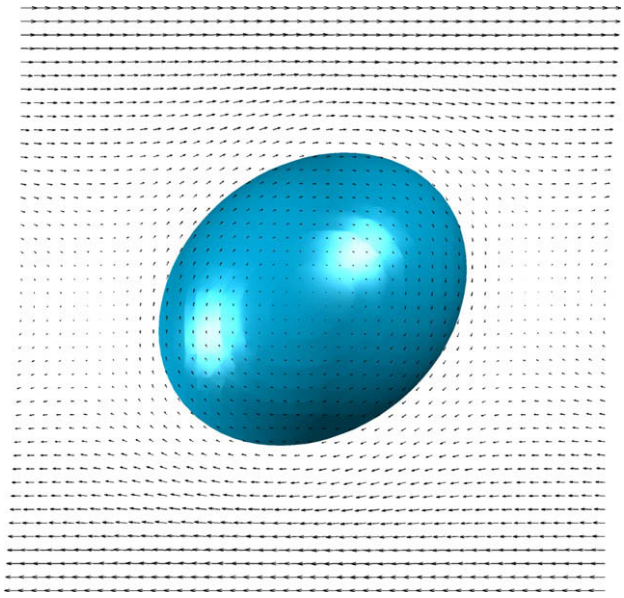

Fig. 2. The two-dimensional velocity profile in the plane [0,0,1] and the droplets iso-contour $C = 0$ at steady-state in a Couette flow.

the daughter branches have a rectangular cross section $L \cdot L_B$, where L is in the z-direction. The daughter to parent channel area is $\frac{L \cdot L_B}{L^2} = 0.75$ and θ is the bifurcation angle. The droplet has initially a volume V_i and the non-dimensional volume is defined as $V = \frac{V_i}{L^3}$. The walls are hydrophobic, having an affinity of the continuous phase, with an equilibrium contact angle of $\theta_e = 180°$. This prevents wetting of the dispersed phase on the channel surfaces. The non-dimensional numbers given in Eq. (16) are defined with the characteristic length scale chosen as the width of the parent channel $L_c = L$ and the reference velocity has been chosen as the mean velocity at the inlet.

Droplets are an important part in microfluidic applications that often consist of complex networks of channels. Microfluidic flows are laminar, but the Re number can be greater than unity (Song et al., 2003) as the droplets traverses through these complex geometries. The focus here is on the detailed droplet dynamics in a generic flow configuration at small scales, a bifurcating channel, rather than simulating a whole microfluidic system. Here the Re number is small, but larger than unity $Re = 14.7$ and $Pe = 1 \times 10^3$, both kept constant in all simulations. These non-dimensional numbers can be interpreted as a flow consisting of two immiscible liquids with, say, material properties similar to water ($\rho = 10^3$ kg/m^3, $\mu = 0.001$ Pa s) with a bulk diffusion coefficient $D_B = 1.47 \times 10^{-8}$ m^2/s. The continuous phase would then have a mean velocity at the inlet $U = 0.0147$ m/s and the width of the parent channel is $L = 1$ mm. These dimensions are typical of many microfluidic systems, see for instance Song et al. (2003), Calderon et al. (2005) and Eshpuniyani et al. (2005). The only material property we vary in the simulations is the surface tension coefficient for the two phases; $1.4 \times 10^{-4} \leqslant \sigma < 7.8 \times 10^{-3}$ ($0.1 > Ca \geqslant 1.8 \times 10^{-3}$).

The channel has an extension in the x-direction of about $10L$. A nearly equidistant mesh has been employed between the inlet and

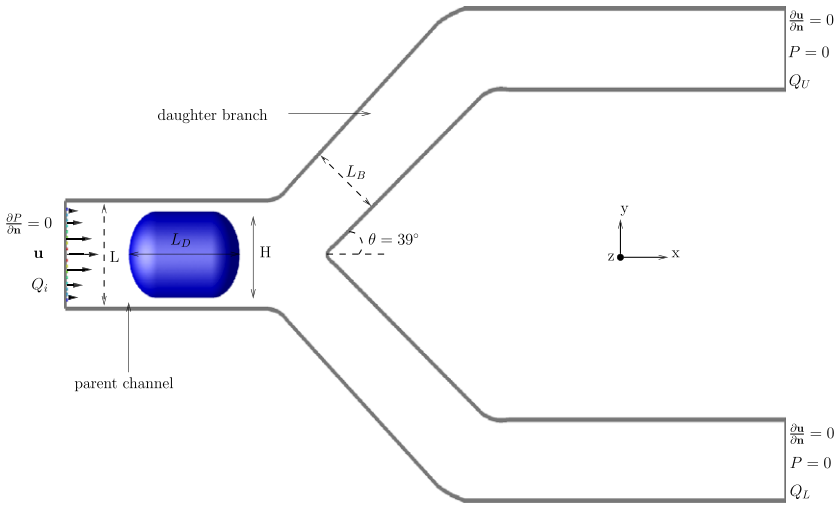

Fig. 3. Geometrical description of the numerical domain.

the straight section (in x-direction) of the branches, with few skewed cells near the point of the bifurcation. L is discretized by 50 node points. In the straight section of the branches, where they are aligned with the x-direction, has a coarse mesh with $L \sim 10$ node points in order to reduce the computational time. The extension of the branches ensures that the droplet behavior is not influenced by the outlet boundary condition in the simulations. The mesh consists of nearly 7.5 million tetrahedron elements and the computational time on 1024 processors for a single case was about 24 h.

3. Freely evolving droplet dynamics

3.1. Flow regimes: splitting and non-splitting

In the quest to identify the parameters that govern the process of droplet splitting or non-splitting in the junction, a set of simulations with different Ca numbers and initial droplet size were performed. Figs. 4–6 displays the three-dimensional droplet isosurface for $C = 0$ and the velocity field in the cross section, taken at the center line in the channel, with a normal $[0 \cdot \bar{e}_x, 0 \cdot \bar{e}_y, 1 \cdot \bar{e}_z]$. In these three simulations the droplets have the same initial shape, as a liquid slug, with the aspect ratio $\frac{L_D}{H} = 2$, a volume $V = 0.67$ and $Cn = 0.06$.

Fig. 4 describes the temporal droplet evolution with its velocity vectors for $Ca = 3.0 \times 10^{-3}$. Fig. 4a shows the elongated droplet as it is just about to come in contact with the edge of the junction. It deforms symmetrically forming two identical liquid fingers in the upper and lower daughter branch, which almost completely fill the channel (Fig. 4b). The droplet rear forms a small curvature, with a large radius, at the entrance of the bifurcation, bulging in the upstream direction (Fig. 4b). A cylindrical liquid thread is formed between the tip of the junction and the droplet rear, which drains symmetrically into the branches, see Fig. 4c. As the circumference of the thread becomes less than its normal length, the surface tension force starts to contract it radially. This eventually results in a pinch-off and the formation of two equally sized daughter droplets, with a spherical shape. The two droplets propagate downstream in the channel branches, and a thin film is formed of the continuous phase, between the channel surface and the droplet interface, see Fig. 4d.

Fig. 5 describes the temporal droplet evolution with its velocity vectors for $Ca = 2.2 \times 10^{-3}$. In comparison with the results in Fig. 5 the capillary force is here just slightly stronger, resulting in an almost identical droplet shape as it approaches the junction (Fig. 5a). Fig. 5b shows the droplet as it has deformed in the junction. Due to the stronger capillary force it has a larger curvature at its rear than observed Fig. 4b. The deformation of the interface converts work done by inertial and viscous forces into surface energy, leading to a deceleration of the droplet at the tip of the junction. Notice that the magnitude of the velocity vectors inside the droplet is smaller in comparison with the outer flow. It stays at the junction until the incipience and growth of an instability similar to the Rayleigh–Plateau (R–P) (Rayleigh, 1882) instability. This instability appears as the length of the liquid thread exceeds its circumference, meaning that its surface area can be reduced by breakup as this is energetically favorable. The instability is here not initiated exactly at the centre of the channel, causing a slight asymmetric drainage of the liquid bridge, with a higher flow rate entering the lower branch (Fig. 5c). Finally, the thread pinches off forming two droplets, where the droplet in the lower branch is slightly larger than the droplet in the upper branch (Fig. 5d).

Fig. 6 describes the temporal droplet evolution with its velocity vectors for $Ca = 1.8 \times 10^{-3}$. By further reducing the Ca number, in comparison with Figs. 4 and 5, through an increase in the surface tension force, we observe a different droplet behavior. Initially, the droplet approaches the junction in a similar fashion as reported above. But the dominating surface tension force reduces the ability of the inertia and viscous force to deform the droplet and it obtains a quasi steady-state condition, with no internal flow, as it sticks in the junction, see Fig. 6a.

Due to the stronger capillary force, a larger curvature is generated at the droplet rear, resulting in a larger radius of the liquid thread. This has a direct consequence on the resulting droplet dynamics, as the birth of a R–P instability is prevented. Although the droplet preserves this state for several hundred time steps, we find this sticking behavior to inherit an unstable nature as the droplet always exits into one branch. The incipience of a numerical disturbance, generates a slightly asymmetric flow in the film formed between the droplet interface and the channel surface, which initiates droplet slipping see Fig. 6b. As the perturbation grows the droplet migrates into the lower daughter branch (Fig. 6c). This leaves an asymmetric distribution of the phases in the daughter branches and the droplet wrapping generates a flow recirculation in the upper branch. For flows with $Re \ll 1$ such recirculation patterns would be absent, as they would be damped by the viscosity. Finally the droplet propagates into the lower branch, see Fig. 6d.

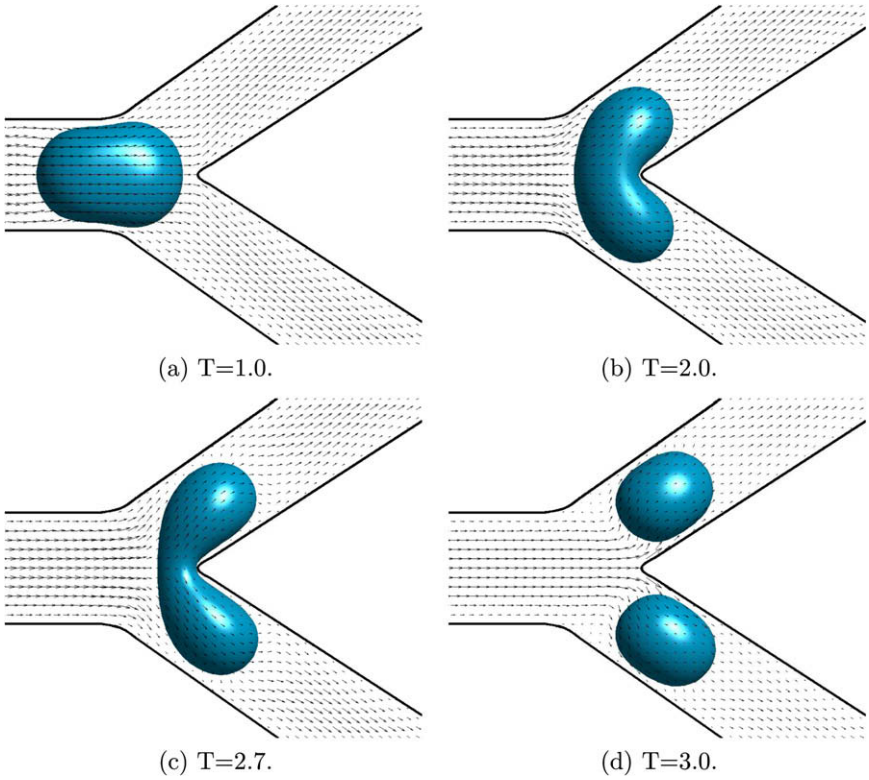

Fig. 4. Droplet dynamics in a bifurcating channel at four different snapshots in time with $Ca = 3.0 \times 10^{-3}$ and $V = 0.67$, in the splitting regime. The figure shows the iso-surface for the order parameter $C = 0$ with $Cn = 0.06$ and the velocity vectors in the plane [0,0,1].

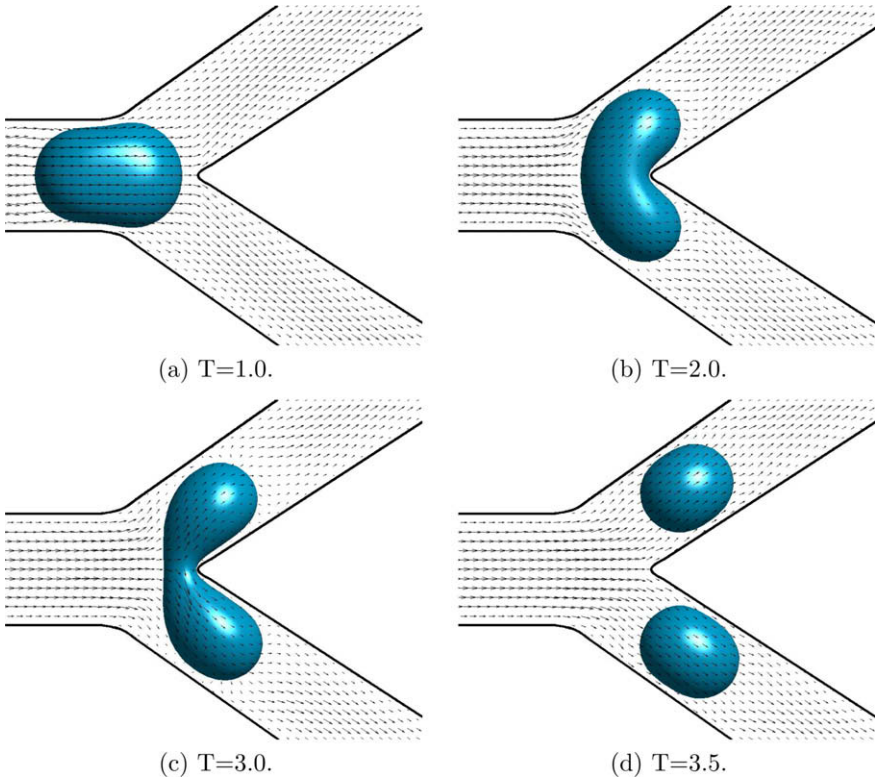

Fig. 5. Droplet dynamics in a bifurcating channel at four different snapshots in time with $Ca = 2.2 \times 10^{-3}$ and $V = 0.67$, in the splitting regime. The figure shows the iso-surface for the order parameter $C = 0$ with $Cn = 0.06$ and the velocity vectors in the plane [0,0,1].

The temporal evolution of the surface area for the three cases reported above are shown in Fig. 7. The vertical axis depicts the non-dimensional droplet surface area, where A_i is the initial droplet area. The droplets have initially the same shape, but different

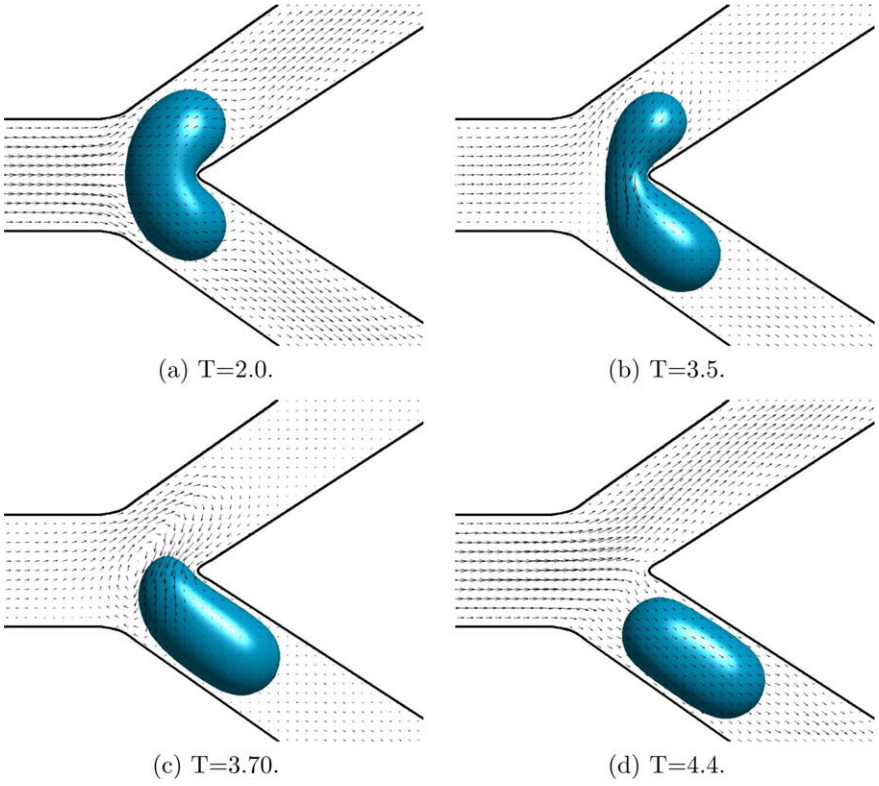

Fig. 6. Droplet dynamics in a bifurcating channel at four different snapshots in time with $Ca = 1.8 \times 10^{-3}$ and $V = 0.67$, in the splitting regime. The figure shows the iso-surface for the order parameter $C = 0$ with $Cn = 0.06$ and the velocity vectors in the plane [0,0,1].

surface tension coefficients. As shown in Figs. 4–6, small variations in the magnitude of the capillary force can have a large influence on the droplets ability to deform in the bifurcation. We notice in Fig. 7 that their initial shape is not being energy minimized, explaining the small deviation from the value one at the first output at $T = 0.1$. As the droplets approach the tip of the bifurcation they deform in a similar manner, with a continuous decrease in surface area. They obtain the same minimum surface area as the major part of the droplet occupies the region, where the channel bifurcates, see Fig. 7 at $T \sim 1.5$. At this place in the channel the droplet is least confined between the walls, so that it attains a shape with a surface area being less than what it had in the parent channel. As the droplets nose interacts with the tip of the junction it deforms into its two branches. This leads to an increase in surface area, where the three droplets deform in a similarly fashion until the time $T = 2$. Around this time, the effect of the different Ca numbers starts to manifest itself. The case with the lowest surface tension force ($Ca = 3 \times 10^{-3}$) has a linear increase in surface area from the time $T = 1.5$ until droplet breakup at $T = 2.8$. An abrupt change in surface area is then observed, demonstrating that splitting is energetically favorable. Afterwards, the two droplets readjust into their equilibrium shape as they propagate into the two daughter branches.

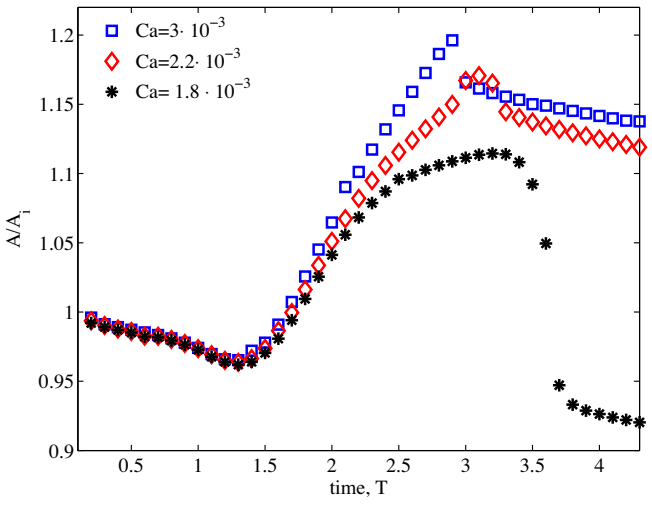

Fig. 7. The temporal evolution of the surface area for three droplets with different Ca number, with $V = 0.67$ and A_i is the initial droplet surface area.

For the case with $Ca = 2.2 \times 10^{-3}$ the slope of the surface area in time becomes different around time $T = 2$. Here the surface force becomes comparable with the inertia and the viscous forces acting on the droplet, which decreases the deformation. The change in Ca changes also the temporal timescale in the flow, and breakup takes place at $T = 3.1$.

The non-splitting droplet ($Ca = 1.8 \times 10^{-3}$) has a different behavior than the two cases with lower surface tension coefficients described above. Its surface area increases up to around time $T = 2.4$, then its growth almost ceases with just a small change in surface area until $T = 3.3$ when the droplet stops at the tip of the bifurcation, see Figs. 6 and 7. Around $T = 3.3$ the droplet starts to wrap into the lower branch, having a large effect on its surface area that rapidly reduces by around fifteen percent between time $T = 3.2$ and $T = 3.7$. As the droplet has migrated into the lower branch it adjusts into its energy minimizing shape, obtaining a lower surface area than it had at time $T = 0$. That its surface area is less in the smaller branch than in the larger parent channel may seem counterintuitive. This is due to that the speed in the channel containing the droplet is decreased, giving a lower local Ca, and thus a smaller droplet distortion.

Q_i, Q_U and Q_L are the mass fluxes through the inlet, upper and lower outlet, respectively, see Fig. 3. Fig. 8 shows how the

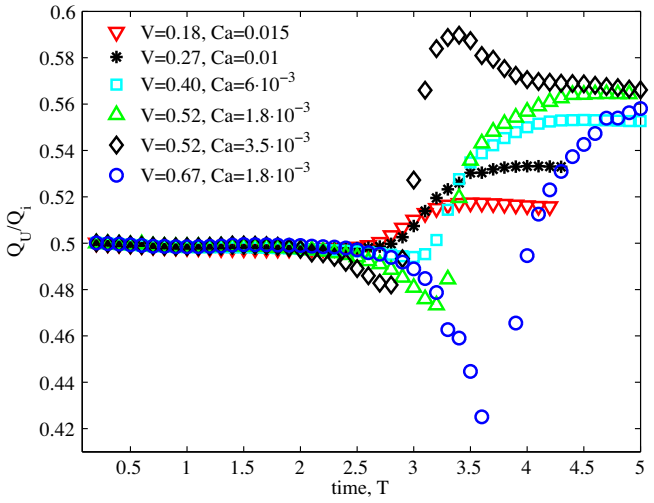

Fig. 8. The mass flow ratio between the upper outflow branch and the inflow, where the vertical axis describe the outflow ratio $\frac{Q_U}{Q_i}$.

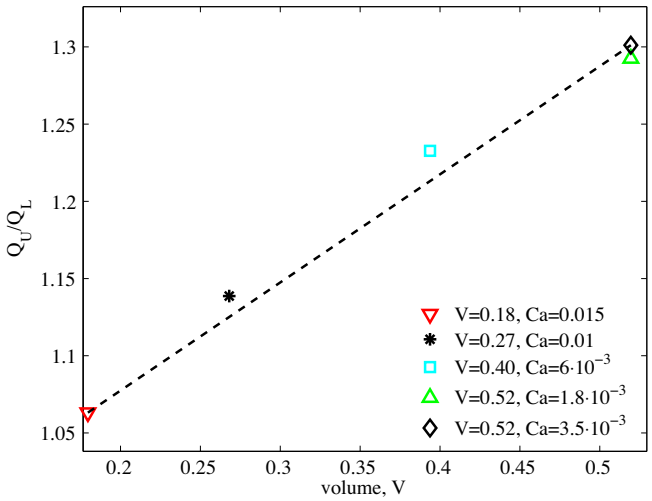

Fig. 9. The droplet volume V is plotted against the mass flow distribution between the upper and lower branch $\frac{Q_U}{Q_L}$. The dotted line is added as a guide to the eye. A linear relationship between the mass flow ratio and volume is found to be approximated to; $\frac{Q_U}{Q_L} = 0.94 + 0.70\,V$.

non-splitting droplets influence the mass flow distribution in the junction. The figure describes the ratio between the outflow in the upper branch (Q_U), which is not occupied by the droplet, and the inflow (Q_i). It should be noted that by monitoring the ratio between the lower branch and the inlet produces a symmetric plot as seen in Fig. 8. The splitting droplets, of equal size, produce a symmetric outflow of the two daughter branches. The asymmetric effect generated by the non-splitting droplets is clearly demonstrated in Fig. 8 and portray that the droplets, although having the same density and viscosity as the continuous phase, acts as a flow resistance in the branch they occupy. This effect is primarily generated by the interface, which is sensed by the outer flow. We note that such an observation has also been made in droplet experiments performed by Garstecki et al. (2005). The blue hollow circles describe the mass flow ratio, in this context, of a large droplet, which does not obtain a steady outflow before entering the section of the branch that is aligned with the x-direction.[1] Nonetheless for smaller droplets one can observe in Fig. 8 that there is a dependence on the droplet size and the distribution of the continuous phase in the two branches. These results reveal that the flow ratio between the upper and lower branch converge towards a constant value, depending on droplet size.

By monitoring the outflow ratio in time we can observe the effect of the perturbation as the droplet wraps into the branch. This is illustrative for the two cases, where the droplet has the same size ($V = 0.52$), but different Ca numbers. For these cases the path to the final outflow distribution between the branches are highly different, but their final value is nearly the same. This also shows, for the parameters space investigated here, that the Ca number plays a minor effect with regard to the outflow ratio, see Fig. 9.

By plotting the final outflow ratio between the upper and lower branch, we find the relationship for the flow resistance that is dependent on the droplet size, see Fig. 9. The outflow ratio is found to depend linearly on the droplets volume, the dashed line in Fig. 9 is described by $\frac{Q_U}{Q_L} = 0.94 + 0.70V$. The large droplet, see blue hollow circles Fig. 8, have been disregarded here as the outflow ratio does not reach steady-state in the branch.

[1] For interpretation of color in Figs. 8 and 10, the reader is referred to the web version of this article.

3.2. Flow regime map

The droplet splitting or non-splitting phenomenon depends mainly on the relative dominance of the surface tension force, represented in the Ca number. The resulting droplet dynamics seem to also highly depend on its initial configuration, identifying the droplet size and the Ca number as two of the key parameters for the definition of the multiphase flow characteristics in the junction. Similar experimental observations have been made in both T- (Link et al., 2004) and λ-junctions (Menetrier-Deremble and Tabeling, 2006; Eshpuniyani et al., 2005). These parameters form a non-dimensional space, which is explored in numerical experiments, describing the relationship between the splitting and non-splitting flow regimes as shown in Fig. 10.

Note in particular that there seem to be a distinct, well-defined, condition for the flow regime transition between splitting and non-splitting droplets. Close to this threshold we recognize that a slight

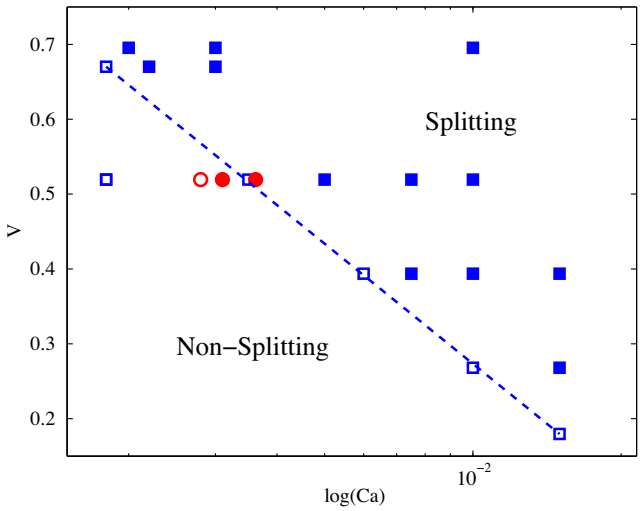

Fig. 10. Semi-logarithmic map of the splitting and non-splitting flow regime, the dotted line has been added as a guide to the eye. The square markers are results with $Cn = 0.06$ and the circles $Cn = 0.08$, hollow markers denote non-splitting and filled markers splitting droplets. The dashed line describes the threshold for splitting or non-splitting approximated by $V = -0.79 - 0.53 \cdot \log(Ca)$.

variation in droplet size or the surface tension force could have a tremendous affect on the flow physics in the junction. These findings identify that large droplets favor splitting and that such a process is hard to obtain with small droplets. Strikingly, the threshold for splitting or non-splitting falls on a single curve given by $V = -0.79 - 0.53 \cdot \log(Ca)$, see Fig. 10.

The red circles in Fig. 10 represent the results for simulations with a thicker interface $Cn = 0.08$. We note that the criterion for splitting and non-splitting changes with the interface width. Close to the splitting/non-splitting threshold it is expected that even small changes in parameters, like the interface width, will have an effect on the results. By reducing the interface width the splitting curve might shift slightly towards higher Ca numbers, although the shape of the curve and the actual interfacial dynamics are not believed to change significantly.

There are some salient points that need to be emphasized. We note that the disturbance initiating droplet motion into the lower branch in the non-splitting regime has a numerical nature. Flows involving droplets that will not split or rigid particles that enter a bifurcation are inherently unstable. Here the droplet always enters the same branch, demonstrating that the perturbation is numerically consistent for all cases. One hypothesis for the perturbations is that there is a slight asymmetry in the mesh near the point of bifurcation. Another explanation could be that this effect is caused by the convergence criteria, even though they are small at each time step ($\epsilon \sim 10^{-7}$) they are of finite size and accumulate in time. In order to quantify the magnitude of the perturbation needed to control the droplet motion, we introduce a small asymmetry between the two outlet boundary conditions. This is done in practice by restarting the simulations from a state when the droplet sticks in the junction, placing a small variation between the pressure outlets. We observed that the droplet change branch when a pressure difference of $\Delta P = \frac{P_{upper} - P_{lower}}{P_{in}} \sim 0.04$ is placed between the two branches, where P_{in} is the inlet pressure at the restarted time step. This indicates the disturbance sensitivity nature of the non-splitting flow regime and illustrates that the symmetric placement of a drop at the junction is highly unstable. Experimentally such unstable two-phase flow phenomena have been observed in similar geometries by Baroud et al. (2006) and Calderon et al. (2005).

4. Conclusion

The present paper reports on three-dimensional numerical experiments based on Phase Field theory of droplet dynamics in a bifurcating channel with symmetric outflow conditions. Two distinct flow regimes are identified as the droplets interact with the junction, splitting and non-splitting. In particular we show the effects of the initial droplet size and Ca number on the resulting two-phase flow characteristics.

Droplets that split equally, produce a symmetric distribution of both phases in the channel daughter branches. Near the threshold between the two regimes, we observe that the R–P instability can be a driving parameter for droplet division.

In the non-splitting regime the droplet migrates into one of the channel branches, leading to a strong temporal asymmetric flow in the junction. A linear relationship is found for the droplet size and the outflow ratio between the upper and lower branch. By placing a small difference between the upper and lower outflow condition we demonstrate the disturbance sensitive nature of the flow. This is illustrating that a symmetric placement of the droplet in the parent channel is highly unstable.

These results identify the Cahn–Hilliard Navier Stokes equations solved with a finite element method as a viable computational platform for the description of multiphase flow characteristics in complex geometries at small scales. One prospect for the future is a further description and identification of novel interfacial dynamics. Future studies should include the influence of the tip geometry, multiple droplet interaction and wettability effects, in order to obtain more pieces of the puzzle forming the physical picture of droplet dynamics in bifurcating channels.

Acknowledgement

Computer time provided by Swedish National Infrastructure for Computing (SNIC) is gratefully acknowledged.

References

Amberg, G., Tonhardt, R., Winkler, C., 1999. Finite element simulations using symbolic computing. Math. Comp. Simulat. 49, 257–274.
Anna, S.L., Bontoux, N., Stone, H.A., 2003. Formation of dispersions using flow focusing in microchannels. Appl. Phys. Lett. 82, 364–366.
Aussillous, P., Quere, D., 2000. Quick deposition of a fluid on the wall of a tube. Phys. Fluids 12, 2367–2371.
Baroud, C.N., Tsikata, S., Heil, M., 2006. The propagation of low-viscosity fingers into fluid-filled branching networks. J. Fluid Mech. 546, 285–294.
Bretherton, F.P., 1961. The motion of long bubbles in tubes. J. Fluid Mech. 10, 166–188.
Bull, J.L., 2005. Cardiovascular bubble dynamics. Crit. Rev. Biomed. Eng. 33, 299–346.
Cahn, J.W., Hilliard, J.E., 1958. Free energy of a nonuniform system. I. Interfacial free energy. J. Chem. Phys. 28, 258–267.
Calderon, A.J., Fowlkes, J.B., Bull, J.L., 2005. Bubble splitting in bifurcating tubes: a model study of cardiovascular gas emboli transport. J. Appl. Physiol. 99, 479–487.
Calderon, A.J., Heo, Y.S., Huh, D., Futai, N., Takayama, S., Fowlkes, J.B., Bull, J.L., 2006. Microfluidic model of bubble lodging in microvessel bifurcations. Appl. Phys. Lett. 89, 244103.
Carlson, A., Do-Quang, M., Amberg, G., 2009. Modeling of dynamic wetting far from equilibrium. Phys. Fluids 21, 121701–121704.
De Menech, M., 2006. Modeling of droplet breakup in a microfluidic t-shaped junction with a phase-field model. Phys. Rev. E, 73.
De Menech, M., Garstecki, P., Jousse, F., Stone, H.A., 2008. Transition from squeezing to dripping in a microfluidic t-shaped junction. J. Fluid Mech. 595, 141–161.
Do-Quang, M., Villanueva, W., Singer-Loginova, I., Amberg, G., 2007. Parallel adaptive computation of some time-dependent materials-related microstructural problems. Bull. Polish Acad. Sci. Tech. Sci. 55, 229–237.
Eshpuniyani, B., Fowlkes, J.B., Bull, J.L., 2005. A bench top experimental model of bubble transport in multiple arteriole bifurcations. Int. J. Heat Fluid Flow 26, 865–872.
Fuerstman, M.J., Garstecki, P., Whitesides, G.M., 2007. Coding/decoding and reversibility of droplet trains in microfluidic networks. Science 315, 828–832.
Garstecki, P., Fischbach, M.A., Whitesides, G.M., 2005. Design for mixing using bubbles in branched microfluidic channels. Appl. Phys. Lett. 86, 86–88.
Guermond, J.L., Quartapelle, L., 1997. Calculation of incompressible viscous flows by an unconditionally stable projection fem. J. Comp. Phys. 132, 12–33.
Jacqmin, D., 1999. Calculation of two-phase Navier–Stokes flows using phase-field modeling. J. Comp. Phys. 155, 96–127.
Link, D.R., Anna, S.L., Weitz, D.A., Stone, H.A., 2004. Geometrically mediated breakup of drops in microfluidic devices. Phys. Rev. Lett. 92. 054503-1–054503-4.
Manga, M., 1996. Dynamics of drops in branched tubes. J. Fluid Mech. 315, 105–117.
Menetrier-Deremble, L., Tabeling, P., 2006. Droplet breakup in microfluidic junctions of arbitrary angles. Phys. Rev. E 74.
Pozrikidis, C., 2001. Interfacial dynamics for Stokes flow. J. Comp. Phys. 169, 250–301.
Prakash, M., Gershenfeld, N., 2007. Microfluidic bubble logic. Science 315, 832–835.
Rayleigh, L., 1882. On the equilibrium of liquid conducting masses charged with electricity. Philos. Mag. 14.
Song, H., Tice, J.D., Ismagilov, R.F., 2003. A microfluidic system for controlling reaction networks in time. Angew. Chem. Int. Ed. 42, 768–772.
Taylor, G.I., 1934. The formation of emulsions in definable fields of flow. Roy. Soc. Lond. Proc. Ser. A 146, 501–523.
Taylor, G.I., 1960. Deposition of a viscous fluid on the wall of a tube. J. Fluid Mech. 10, 161–165.
van der Graaf, S., Nisisako, T., Schroen, C.G.P.H., van der Sman, R.G.M., Boom, R.M., 2006. Lattice Boltzmann simulations of droplet formation in a t-shaped microchannel. Langmuir 22, 4144–4152.
van der Waals, J., 1893. The thermodynamic theory of capillarity under the hypothesis of a continuous variation of density. J.D. Verhandel. Konink. Akad. Weten. 1 (J. Stat. Phys., 20, 1979 (in English)).
Villanueva, W., Amberg, G., 2006. Some generic capillary-driven flows. Int. J. Multiphase Flow 32, 1072–1086.